AJEMA GLOBAL RESEARCH NETWORK

AMERICAN Journal of Engineering, Mechanics and Architecture
Volume 3, Issue 10, 2025 ISSN (E): 2993-2637

Three-Dimensional Unsteady Analysis of Fluid–Structure Interaction in Check Valves of Diaphragm Volumetric Pumps

Ali Shakir Hial Alaqra

Abstract: A comprehensive unsteady three-dimensional numerical model employing dynamic meshing techniques has been developed to simulate the fluid–structure interaction (FSI) occurring within the non-return valves of air-operated diaphragm pumps. This advanced 3D CFD model offers a more precise representation of flow dynamics and a more accurate assessment of valve motion behavior compared to the earlier 2D model previously introduced by the authors. The improved model particularly enhances the understanding of internal volumetric losses caused by valve movement, which negatively impact the overall efficiency of the pump.

The study investigated both piston-type and deformable diaphragm geometries under sinusoidal displacement conditions. Results showed comparable performance in terms of basic pump functionality for both configurations. Detailed simulations under normal operating and free-discharge conditions revealed increased instability in the check valves when the supplied air pressure was low.Notably, the exhaust valve exhibited significant valve "tapping," characterized by repeated partial closures during the forward stroke due to strong fluid–structure interactions. In contrast, the intake (aspirating) valve demonstrated more stable sealing behavior, with only minor reopening observed at the onset of the backward stroke.These numerical insights have proven valuable for pump manufacturers, informing improvements in valve design, material selection, and maintenance strategies. The findings have directly contributed to the development of new and more efficient pump prototypes

Keywords: 3D CFD modeling, Air-operated double diaphragm pump, Dynamic mesh, Fluid–Structure Interaction (FSI), Ball valve tapping.

1. Introduction

A diaphragm pump is a type of positive displacement machine that transfers fluid by flexing an elastic membrane (the diaphragm). It typically handles highly viscous fluids and relies on a pair of non-return (check) valves to prevent backflow during operation. Among these, air-operated diaphragm pumps are particularly common; they use a dual-diaphragm configuration with four check valves, driven by compressed air through a shuttle valve system that alternates the diaphragm movement. These systems are widely referred to as Air-Operated Double Diaphragm (AODD) pumps.

In this configuration, the elastomeric diaphragm serves a dual purpose: it creates a reciprocating motion to move the fluid and simultaneously acts as a dynamic seal. This eliminates common problems found in other pump types, such as internal leakage, abrasive wear, and the need for lubrication. However, the check valves in AODD pumps remain vulnerable to mechanical degradation, including worn valve balls, deformed seats, misaligned guides, and damaged o-rings—typically resulting from high-cycle fatigue.

Traditionally, the development of AODD pumps has relied heavily on experimental methods to evaluate performance, ensure material compatibility, and assess pump durability under various operating conditions [1,2]. Industry standards [2] are available to guide this process. However, most design improvements have historically emerged from trial-and-error methods, often inspired by competitor designs and incorporating only minor, proven changes.

Given the increasing demand for rapid and cost-effective prototype evaluation, modern simulation tools—especially Computational Fluid Dynamics (CFD)—are now essential in pump development. In this context, SAMOA Industrial S.A. [3,4], a leading European manufacturer of fluid-handling equipment, has introduced a new generation of AODD pumps featuring a re-engineered internal layout. Their design leverages CFD simulations to assess and optimize pump performance at the prototyping stage.

In a previous study by the authors [5], a novel CFD methodology was presented to analyze diaphragm pump performance using a deformable mesh technique. This allowed simulation of the diaphragm's full unsteady motion and detailed modeling of the fluid–structure interaction (FSI) between the fluid and the check valve balls. Similar numerical methods have also been applied in the analysis of other types of positive displacement pumps, including axial piston pumps [6], air-operated piston pumps [7], plunger pumps [8], and vane pumps [9]. Researchers have further investigated the suction characteristics and geometric optimization of these machines [10,11], along with the effects of non-Newtonian fluid behavior [12].

More recent efforts have combined these CFD models with cavitation simulations to better understand suction phenomena [13,14]. A significant research focus now lies in modeling the dynamic behavior of check valves and their interaction with the diaphragm or piston motion. To this end, transient FSI simulations have become widely used in analyzing reciprocating pumps with non-return valves. Initial studies modeled the ball motion using deformable grids [15] to simulate high-pressure safety valves [16], ball valves [17], and disk valves [18]. Advanced studies now investigate the behavior of discharge valves within full 3D pump geometries, such as plunger pumps [19] and reciprocating piston pumps [20].

Parallel developments have applied similar techniques to linear [21] and rotary compressors [22,23], using software tools like ANSYS Fluent® and ADINA®. In contrast, very few CFD studies exist on diaphragm pumps. One exception is a simulation of a piston-diaphragm pump with spring-loaded check valves using an immersed boundary method and FSI modeling [24], while another recent study analyzed spring-loaded port valves in a diaphragm pump [25]. These studies simplify the numerical problem by incorporating spring stiffness, which restricts ball displacement and improves convergence. However, in the absence of springs, physical stoppers must be modeled, as described by the authors in [5], with precise control over the time-step size to ensure numerical stability and accuracy.

The earlier 2D simulations produced results in good agreement with experimental data and demonstrated the value of spatial flow analysis in understanding valve dynamics. In the current work, this methodology is extended to a full 3D simulation of the diaphragm pump. An implicit scheme is used for both mesh motion and the governing fluid equations, adopting an Unsteady Reynolds-Averaged Navier–Stokes (URANS) approach with the RNG k–ε turbulence model.

Initially, the diaphragm's volumetric displacement is modeled using an equivalent cylindrical piston that delivers the same stroke volume. High-resolution meshes are implemented near the valve seats to accurately capture the fluid–structure interaction between the flow and the check valves at various stages of the pumping cycle. Both previous 2D and new 3D results are compared under high and low-pressure operating conditions, evaluating global pump behavior and localized valve responses—specifically focusing on oscillations and valve tapping.

Finally, the study presents an enhanced model that incorporates the actual 3D geometry of the deforming diaphragm, showing comparable performance to the simplified piston approach. The full 3D simulation reveals significant flow recirculations and rotational flow components in the

discharge manifolds, along with oscillatory motion of the check valve balls, associated leakage flows, and time delays in valve opening and closing—all fully resolved using CFD techniques.

2. Air-Operated Double Diaphragm Pump: Geometry and Performance Overview

The pump analyzed in this study is the DP-200, a commercially available AODD pump from a newly developed series by SAMOA Industrial S.A., a global leader in fluid transfer technology and volumetric pump design [26]. This model features a redesigned central layout of internal flow channels, aimed at improving performance and reliability.

Figure 1 presents an exploded view of the pump's key components, including the check valves with their balls, rings, and seats; the central connecting rod between the two diaphragms; and the internal cavities responsible for generating the pulsating discharge flow. The pump operates with a dual-diaphragm mechanism driven by alternating air pressure, producing a balanced and continuous flow. Essential geometrical dimensions and technical specifications of the DP-200 pump are summarized in Table 1. Additional details regarding the re-engineering of this pump series, including design choices and performance validation, are provided in [5]

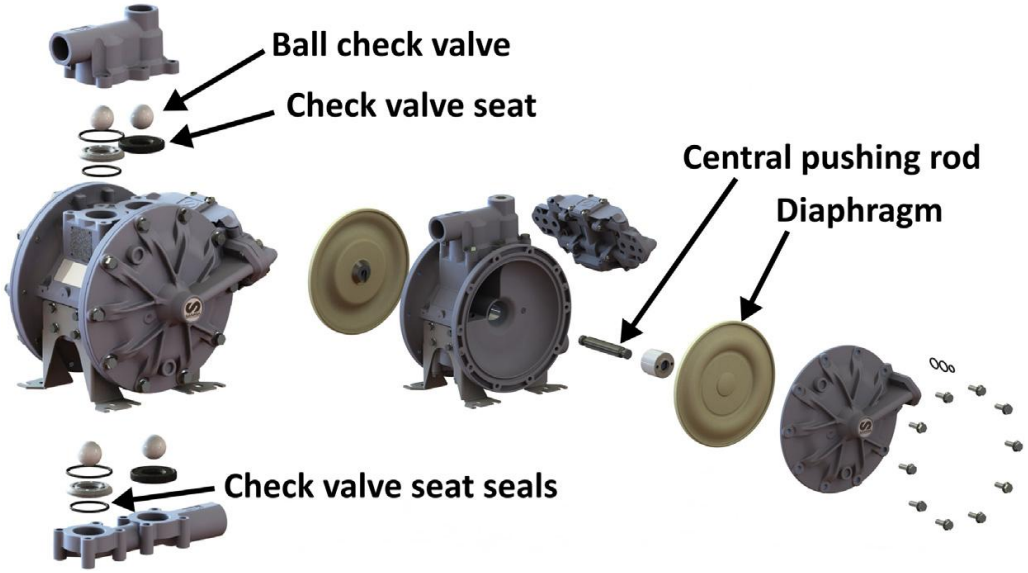

Fig. 1. DP-200 pump: 3D view of the operative components

Table 1. Geometrical data and operating parameters

Diaphragm external diameter, D_e (mm)	200
Diaphragm internal diameter, D_i (mm)	100
Diaphragm effective diameter, D_d (mm)	150
Diaphragm stroke length, L_d (mm)	31.0
Diaphragm effective area, A_d (cm^2)	176.7
Delivery per stroke, V_d (cm^3)	548
Internal manifolds diameter, D_m (mm)	26.5
Ball diameter of check valves, D_v (mm)	31.75
Ball maximum displacement, L_v (mm)	10
Check valve effective area (max), A_v (cm^2)	4.98
Air-operation pressure, P_{air} (bar)	0–8
Pressure ratio (−)	1:1
Maximum free delivery (8 bar), Q (l/min)	200
Maximum driven velocity, n (Hz)	3.0

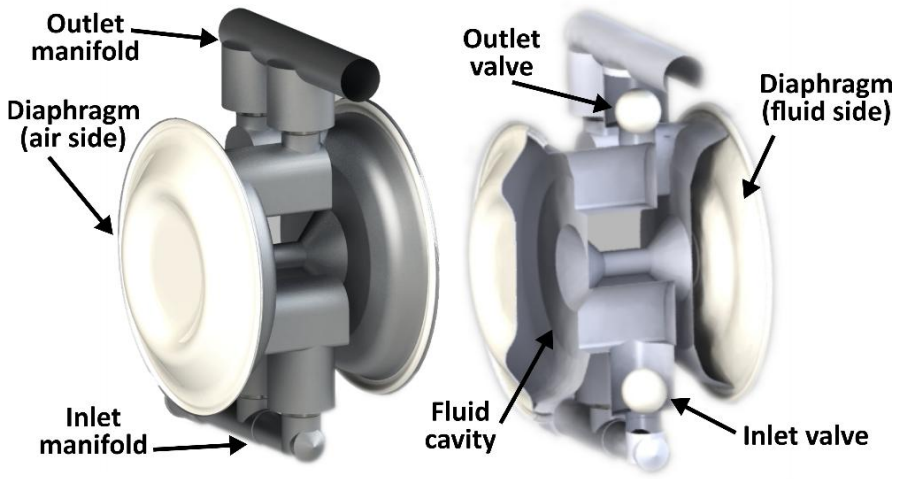

Figure 2. DP-200 pump: Rendered view of cavities and flow passages.

For the purposes of numerical modeling in this study, a three-dimensional representation of the internal flow passages and cavities of the pump was developed, as illustrated in Figure 2. The diagram on the left identifies the key components required to replicate the operational principles of the AODD pump, while the diagram on the right delineates the computational domain selected for discretization. Leveraging the pump's geometrical symmetry, only one half of the full assembly—including a single diaphragm and its corresponding set of check valves—was modeled, thereby optimizing computational efficiency without compromising accuracy.

To conclude this section, the pump's performance curves, extracted from the manufacturer's technical datasheet, are presented in Figure 3. The experimental evaluation was conducted under air supply pressures of 2, 4, and 6 bar, across a range of outlet pressures regulated via a throttle valve positioned in the discharge manifold. Pressure measurements were obtained using two TE Connectivity MEAS U5244 transducers, each with an uncertainty of ±1% over a measurement range of -1 to 13 bar. The corresponding flow rates were determined volumetrically using an electronic balance, resulting in maximum estimated uncertainties of ±0.12 bar in pressure and ±0.7% in flow rate.

The experimental data points are represented by black dots and have been fitted with linear trendlines (solid black lines, referenced to the left y-axis). Additionally, air consumption was recorded using a Testo 6442 thermal flowmeter, capable of measuring within a range of 12 to 3750 liters per minute and featuring a precision of ±0.3%. Efficiency isolines (thin grey lines) are also included in the figure, indicating the pump's operating efficiency under varying conditions.

Furthermore, pressure within the hydraulic chamber was monitored using an ESI Genspec GS4002 transducer, selected for its extended operating range (-1 to 24 bar) to prevent sensor damage from sudden pressure spikes. This sensor also maintains an uncertainty of ±1%, ensuring reliable readings even under dynamic operating conditions.

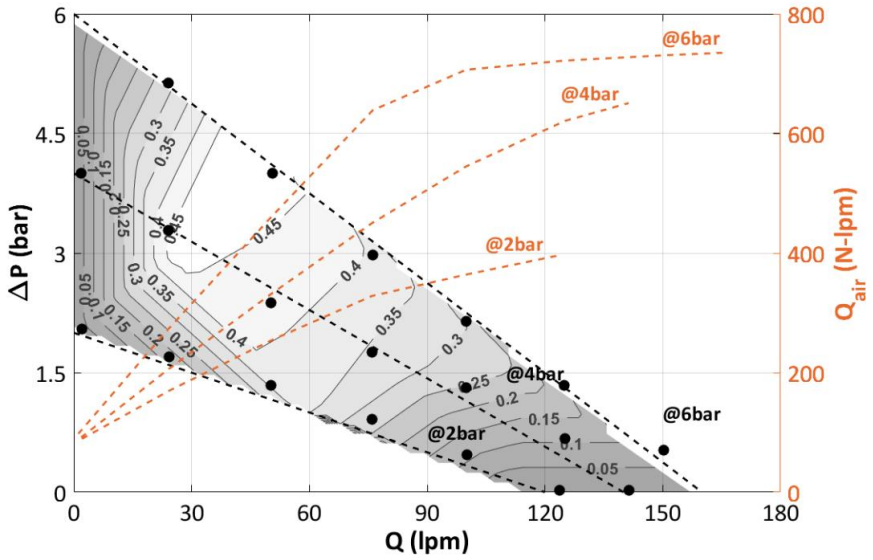

Figure 3. ***DP-200 Pump: Experimental performance curves at varying air-supply pressures.***

3. Three-Dimensional Numerical Model

The numerical simulations presented in this study were performed using the commercial CFD software ANSYS Fluent® v16.2 [27], which solves the Unsteady Reynolds-Averaged Navier–Stokes (URANS) equations through the Finite Volume Method (FVM). The three-dimensional modeling captures both the oscillatory motion of the diaphragm and the flow-induced displacement of the check valve balls. These dynamics were handled via the dynamic mesh capability in Fluent, employing a combination of remeshing and layering algorithms.

To ensure accurate simulation of fluid–structure interactions (FSI), user-defined functions (UDFs) were developed and integrated into the solver. These UDFs implement custom implicit coupling algorithms [28], improving both the convergence rate and overall numerical stability of the FSI solution.

3.1. 3D Geometry and Structured Mesh for a Piston-Equivalent Diaphragm

To reduce computational cost during early stages of model development, a simplified 3D representation was adopted by replacing the actual deformable diaphragm with an idealized, non-deformable piston-like surface that delivers the same volumetric displacement per cycle. An equivalent diaphragm diameter was derived to preserve the stroke volume, allowing for a geometrically simpler, yet hydraulically consistent, modeling approach.

The computational domain was constructed using ANSYS ICEM CFD® v16.2 [29], applying a rectangular block-based strategy. The geometry was decomposed into multiple structured blocks, facilitating the generation of a structured mesh across the entire domain. This modular, body-fitted meshing approach allows for enhanced control over element quality, especially in critical flow regions such as valve seats and narrow passages.

The mesh design followed best practices established in the authors' previous 2D modeling efforts [30], including local refinement near wall boundaries and in tight gaps around valve components. Particular attention was given to the meshing of regions surrounding the valve balls to ensure that dimensionless wall distance (y^+) values remained within an optimal range (4–9) throughout the operating cycle, thus supporting accurate near-wall turbulence modeling.

For the simplified piston-like diaphragm, a layering remeshing technique was applied to accommodate the linear, reciprocating motion of the stroke. The mesh zone adjacent to the moving piston dynamically adjusts during simulation—either expanding or collapsing depending on the stroke position. This dynamic layering process operates under a split factor of 0.4 (new

layers added when local cell height exceeds 140% of the original) and a collapse factor of 0.2 (layers removed when compressed to less than 20% of the initial cell size).

The final 3D mesh consisted of 111,575 hexahedral cells. Figure 4 presents the mesh distribution in the region of the diaphragm and the adjacent inlet and outlet manifolds. A cross-sectional view also illustrates the mesh quality around the valve balls, highlighting the refinement and resolution achieved in these dynamically critical areas

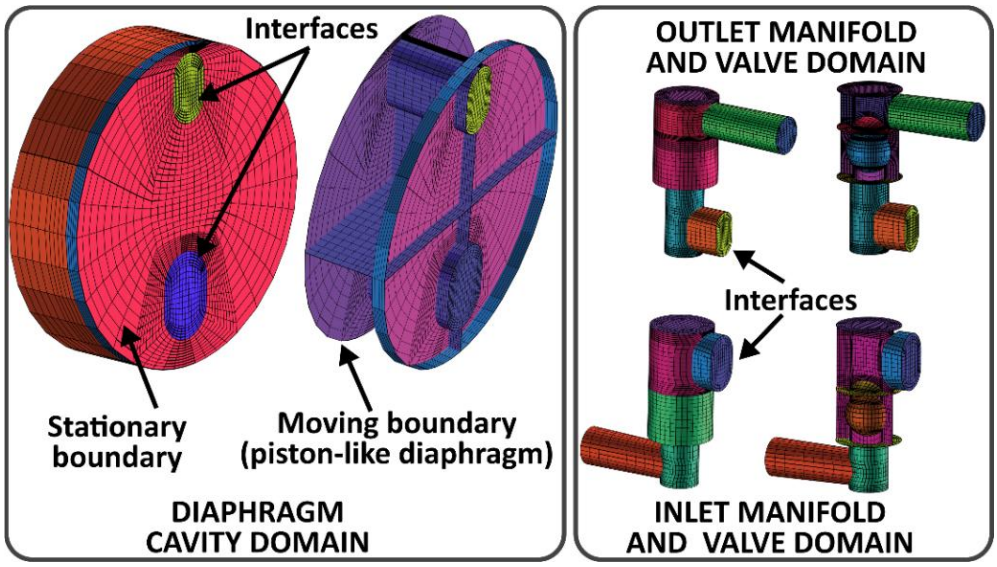

Figure 4. ***Mesh distribution in the piston-like diaphragm and the inlet/outlet manifolds featuring non-return valves.***

Complementing this, Figure 5 provides additional insights into the mesh configuration. The left panel displays the dynamic zones where cells are either created or removed as part of the layering remeshing algorithm, while the right panel offers a global view of the complete structured mesh used in the simulation domain.

The figure also highlights the main boundary conditions applied in the numerical model. At the inlet, a total pressure boundary condition of zero gauge pressure is prescribed. At the outlet, a pressure drop is defined as a function of the kinetic energy, adjusted via a constant KvK_vKv, which simulates different levels of restriction imposed by the throttle valve and thus emulates a range of operational scenarios.

The motion of the piston-like diaphragm is imposed through a compiled user-defined function (UDF) that assigns a sinusoidal velocity profile to the movement of the diaphragm's center of gravity, described by:

v(t)=−πfLdsin⁡(2πft)v(t) = -\pi f L_d \sin(2\pi f t)v(t)=−πfLdsin(2πft)

where LdL_dLd is the stroke length and fff is the actuation frequency.

Additionally, the fluid–structure interaction (FSI) of the valve balls is modeled using a dedicated UDF. This function computes the net hydrodynamic forces acting on the balls at each time step and updates their positions accordingly. Further implementation details for these UDFs are provided in the authors' previous publication [5].

Figure 5. *Left: Remeshing zones for dynamic cell creation/removal. Right: Global view of the structured mesh with boundary conditions and valve positions*

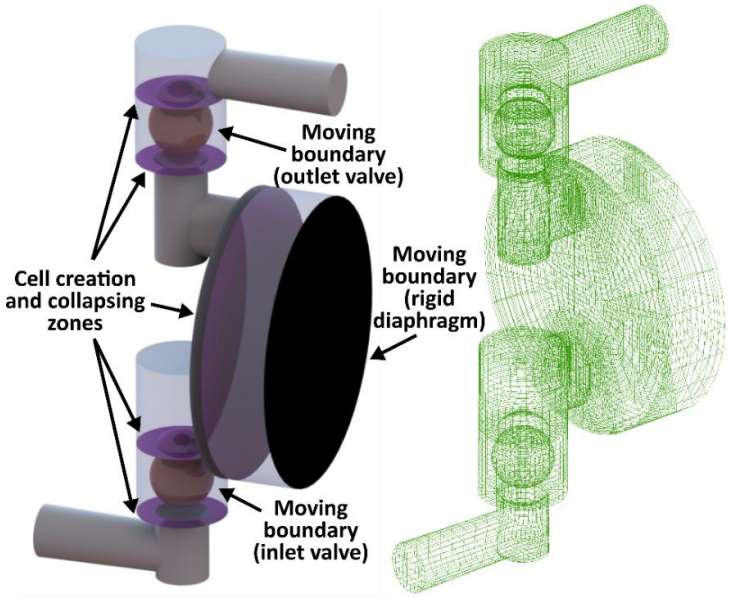

Figure 5. Mesh density in the piston-like membrane and inlet/outlet manifolds with adaptive layering mesh for the balls motion.

3.2. Numerical model and solver

The full 3D model of the pump, using deformable mesh functionalities, has been implemented in the ANSYS-FLUENT solver to resolve the unsteady RANS equations assuming incompressible, viscous flow of a single-phase Newtonian fluid (water):

- Continuity equation:

$$\frac{\partial \bar{u}_i}{\partial x_i} = 0 \qquad (1)$$

- Momentum equation:

$$\rho\frac{\partial \bar{u}_i}{\partial t} + \rho\frac{\partial(\bar{u}_i\bar{u}_j)}{\partial x_j} = -\frac{\partial \bar{p}}{\partial x_i} + \mu\nabla^2\bar{u}_i + \frac{\partial \tau_{ij}}{\partial x_j} \qquad (2)$$

/here the Reynolds Stress Tensor in the momentum equation has been modelled using
ı Eddy Viscosity Model, according to:

$$\tau_{ij} = -\rho\overline{u_i u_j} = \mu_t \underbrace{\left(\frac{\partial \bar{u}_i}{\partial x_j} + \frac{\partial \bar{u}_j}{\partial x_i}\right)}_{S_{ij}} - \frac{2}{3}\rho k\delta_{ij} \qquad (3)$$

In the turbulence modeling framework, the turbulent kinetic energy is denoted by kkk, and the turbulent viscosity is represented accordingly, with a turbulence model constant Cμ=0.0845C_\mu = 0.0845Cμ=0.0845. For turbulence closure, the well-established two-equation RNG k-εk\text{-}\varepsilonk-ε model has been employed due to its recognized robustness and adaptability to a wide range of flow conditions. Preliminary sensitivity studies conducted with the Realizable k-εk\text{-}\varepsilonk-ε model yielded results that were nearly identical to those obtained with the RNG formulation—particularly in terms of valve dynamics and internal flow structures. In contrast, complementary tests using low-Reynolds-number k-ωk\text{-}\omegak-ω models showed excessive numerical damping, which suppressed important flow instabilities associated with the oscillation and tapping behavior of the check valve balls. As a result, the k-ωk\text{-}\omegak-ω family of models was deemed unsuitable for this specific application [5].

For the RNG k-εk\text{-}\varepsilonk-ε model used in this work, and neglecting any buoyancy effects, the closure equations take the following form

$$\rho\frac{\partial k}{\partial t}+\rho\frac{\partial(k\overline{u_i})}{\partial x_i}=\frac{\partial}{\partial x_j}\left[\alpha_k\mu_t\frac{\partial k}{\partial x_j}\right]+2\mu_t S_{ij}S_{ij}-\rho\varepsilon \quad (4)$$

$$\rho\frac{\partial \varepsilon}{\partial t}+\rho\frac{\partial(\varepsilon\overline{u_i})}{\partial x_i}=\frac{\partial}{\partial x_j}\left[\alpha_\varepsilon\mu_t\frac{\partial \varepsilon}{\partial x_j}\right]+C_{\varepsilon 1}\frac{\varepsilon}{k}(2\mu_t S_{ij}S_{ij})-\rho C_{\varepsilon 2}\frac{\varepsilon^2}{k} \quad (5)$$

Where the turbulent dissipation rate is defined as $\varepsilon=2\nu\overline{s'_{ij}s'_{ij}}$, being $s'_{ij}=\frac{1}{2}\left(\frac{\partial u'_i}{\partial x_j}+\frac{\partial u'_j}{\partial x_i}\right)$; and typical coefficients $C_{\varepsilon 1}=1.42, C_{\varepsilon 2}=1.68$ and $\alpha_k=\alpha_\varepsilon\sim 1.383$ have been employed.

A second-order upwind scheme was selected for the discretization of the convective terms, ensuring a balance between numerical accuracy and stability. For the diffusive terms in the momentum equations, Green-Gauss cell-based gradient reconstruction was employed to calculate spatial gradients. The transport equations for both the turbulent kinetic energy (kkk) and the turbulent dissipation rate (ε\varepsilonε) were also discretized using a second-order scheme to maintain consistency in numerical accuracy across the turbulence model.

A segregated solver was adopted, utilizing the PISO (Pressure-Implicit with Splitting of Operators) algorithm, which proved to offer a favorable trade-off between computational cost and numerical robustness. The convergence criteria were set to a residual of 10−610^{-6}10−6 for the continuity equation, and a minimum threshold of 10−510^{-5}10−5 for the implicit mesh motion solver. Both criteria were required to be satisfied before advancing to the next time step, ensuring high fidelity in both fluid flow and mesh deformation.

Time step sizes were carefully selected within the range of 5×10−55 \times 10^{-5}5×10−5 to 1×10−41 \times 10^{-4}1×10−4 seconds, optimizing the balance between computational stability and efficiency. These values were chosen to maintain a Courant number below unity throughout the domain, preventing the numerical wave propagation from outpacing the physical fluid motion, which is especially critical in narrow regions near the check valves undergoing significant mesh deformation.

Table 2 summarizes the main simulation parameters used across the computational database. Notably, smaller time steps were required in cases involving higher operating frequencies and supplied air pressures, due to increased fluid accelerations and valve dynamics. Furthermore, simulating a complete pump cycle typically required around 10,000 time steps per case.

In terms of computational resources, each full-cycle 3D simulation—based on a mesh containing approximately 111,575 cells—required approximately 450 CPU hours, equivalent to 3–4 weeks of wall-clock time, when run on a single workstation equipped with a 4-core Intel Core i7-5820K processor (3.3 GHz) and 64 GB of RAM

Table 2. Numerical database. Outlet BC and time step sizes.

Test No.	Supplied pressure (bar)	Discharge pressure, P_{RMS} (bar)	Loss coefficient, K_v (-)	Driving frequency (Hz)	Time step, Δt (s)	N° time steps per cycle (-)
#1	2	0	0	1.85	$1\text{-}10^{-4}$	5,400
#2	2	1.16	75.1	1.0	$1\text{-}10^{-4}$	10,000
#3	4	0	0	2.45	$1\text{-}10^{-4}$	4,080
#4	4	1.99	62.1	1.4	$1\text{-}10^{-4}$	7,140
#5	4	3.65	1411	0.45	$1\text{-}10^{-4}$	22,220
#6	6	0	0	2.7	$5\text{-}10^{-5}$	7,400
#7	6	1.97	32.5	1.8	$5\text{-}10^{-5}$	11,110
#8	6	3.63	139.9	1.25	$1\text{-}10^{-4}$	8,000
#9	6	4.14	500.8	0.75	$1\text{-}10^{-4}$	13,330

3.3. Three-Dimensional Model with Deformable Diaphragm

To further enhance the physical fidelity of the simulation, an extended modeling approach was developed to incorporate the realistic deformation of the diaphragm in the 3D numerical model. In this configuration, the previously idealized piston-like membrane was replaced by a more physically representative diaphragm, consisting of a rigid central circular plate surrounded by a flexible annular region (see Figure 6). The rigid central plate undergoes sinusoidal displacement, identical to the motion prescribed in the earlier simplified model, while the deformable annulus dynamically adjusts its shape based on radial position to maintain geometric continuity and structural integrity.

Due to the complex deformation of the flexible region, the working chamber required a transition from a structured mesh to a fully tetrahedral mesh, which was managed using an automatic remeshing strategy. This method integrates a spring-based smoothing algorithm by default, which redistributes mesh nodes when boundary displacements are relatively small. However, when large displacements occur—particularly in regions with fine cells—the mesh can suffer from excessive skewness or aspect ratio deterioration, leading to numerical instability.

To mitigate this issue, any cells violating mesh quality criteria (e.g., skewness or size thresholds) were flagged, agglomerated, and remeshed, while the solution variables were interpolated from the original cells. For this process, a spring factor of 0.9 was adopted, with cell sizes constrained between 2 mm (minimum) and 10 mm (maximum), and a maximum allowable cell skewness of 0.7. The mesh update routine was executed every 10 time steps to maintain mesh quality throughout the simulation.

The baseline mesh for this deformable diaphragm model comprised a hybrid unstructured grid with a total of 101,957 elements. Despite containing approximately 10% fewer cells than the piston-like diaphragm model, the computational cost was significantly higher. Specifically, completing a single full working cycle required approximately 550 hours of CPU time on the same workstation—an Intel Core i7-5820K (3.3 GHz, 4 cores, 64 GB RAM). After normalizing the difference in cell count by applying a correction factor of 1.1, the remeshing technique was found to be approximately 30% slower than the layering approach used in the piston-like model.

Given this substantial increase in computational cost, the implementation of a deformable diaphragm is justified only when notable discrepancies in the simulation results are observed between both modeling approaches. To assess the significance of such differences, a set of free-delivery conditions was selected for comparison, corresponding to Test Cases #1, #3, and #6 as listed in Table 5

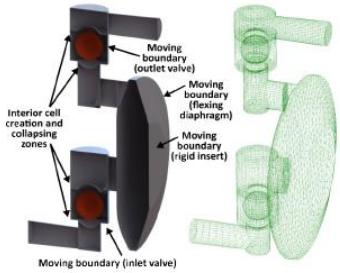

Figure 6. Mesh density in the deformable diaphragm and inlet/outlet manifolds with adaptive layering mesh.

4. Results and Discussion

4.1. Comparison of Performance Curves

To begin the analysis, the predicted flow rate from the 3D numerical model is compared against experimental measurements in Figure 7, where the delivered flow rate is plotted as a function of the discharge pressure. Due to the symmetrical boundary conditions applied in the simulations—

where only one half of the pump geometry was modeled—the computed flow rates were doubled for a direct comparison with experimental values representing the full pump cycle.

The results demonstrate that the numerical model effectively captures the linear decline in flow rate observed in experimental data as the discharge pressure increases. For low to moderate air-supply pressures (2 and 4 bar), the model exhibits good agreement, with maximum relative errors not exceeding 6%, as detailed in Table 3.

At a higher supply pressure of 6 bar, while the general trend of the flow rate reduction is still reasonably replicated, the model shows larger deviations, with maximum discrepancies reaching approximately 19%. These differences are primarily attributed to the increased influence of high air pressure on stroke stability, particularly its effect on the diaphragm dynamics and valve response. This phenomenon, along with its implications for valve instabilities and ball tapping, will be further addressed in the following sections

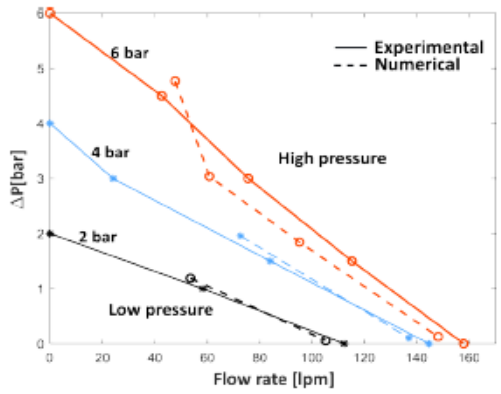

Figure 7. Comparison of experimental and numerical performance curves.

4.2. Pressure Evolution in the Working Chamber

The transient pressure variation within the diaphragm's working chamber is presented for two representative cases in Figure 8, juxtaposing the numerical predictions with corresponding experimental measurements. For reference, previously published results from a 2D numerical model are also included to provide a comparative context.

The left panel illustrates the pressure evolution under conditions of high air-supplied pressure (6 bar) combined with a relatively low discharge pressure (1.5 bar) at the outlet. Conversely, the right panel depicts the pressure response for a scenario with low air-supplied pressure (2 bar) and similarly low exhausting pressure (1 bar).

It is important to highlight that the experimental pressure data were obtained through an ensemble-averaging process over more than 20 operating cycles, thereby effectively reducing the noise and enhancing the reliability of the signal for comparison purposes

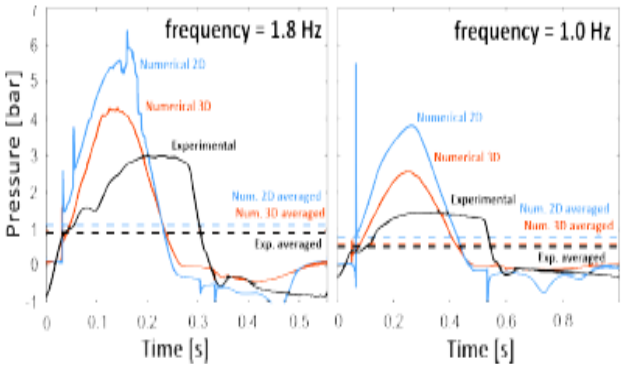

Figure 8. Comparison of experimental and numerical pressure evolutions within the working cavity at high (left) and low (right) air-supplied pressures under standard operation conditions.

The 3D numerical results demonstrate a notably higher fidelity in replicating the pressure evolution inside the diaphragm cavity compared to 2D simulations. Under more demanding conditions (left plot), the experimental pressure profile exhibits a markedly sinusoidal shape, highlighting a significant bidirectional interaction between the air-supplied pressure and the diaphragm dynamics. This interaction likely contributes to the larger discrepancies observed in the pump performance curves. While the numerical pressure follows a sinusoidal pattern imposed by the prescribed piston motion, the 2D model exhibits greater instabilities and reduced accuracy. Importantly, the root mean square (RMS) values of the pressure fluctuations (indicated by dashed mean lines) in the cavity closely match between the experimental data and the 3D simulation, whereas the 2D model overpredicts this value.

In contrast, for low air-supplied pressure conditions (right plot), the experimental pressure displays a stepped profile rather than a smooth sinusoidal waveform. This suggests a reduced influence of hydraulic conditions on the instantaneous supplied air pressure, lending support to the assumption of a sinusoidal membrane motion adopted in both 2D and 3D models. Again, a strong agreement is observed between the time-averaged pressures from experimental and 3D numerical results, while the 2D model overestimates both the mean pressure and exhibits pronounced pressure peaks during valve opening and closing.

Subsequent sections will analyze in detail the internal flow structures and the dynamic response of the pump's components under both high (6 bar, approximately 1.8 Hz) and low (2 bar, approximately 1.0 Hz) air supply pressures. Operating outlet pressures ranging from 1.0 to 1.5 bar, corresponding to standard operational conditions, as well as free-delivery scenarios, will be discussed.

4.3. Standard Operation: Comparison of 2D and 3D Results

Air-operated double diaphragm (AODD) pumps typically operate within an outlet pressure range of 1.0 to 1.5 bar, despite associated efficiency penalties. This operating window is often referred to as "standard operation" by manufacturers and is prevalent in industrial applications of diaphragm volumetric pumps. The following analysis presents the internal pump behavior during conditions of both high and low delivered flow rates.

4.3.1. Delivered Flow Rate and Response of Non-Return Valves

Figure 9 presents a comparison between 2D and 3D model results of flow rate evolution, cavity pressure, and the unsteady response of non-return valves over a typical operating cycle at high driving frequency. The 2D results (left subplots) display sharp pressure spikes within the cavity, partially damped in the outlet pressure, and an unrealistic pressure bump between 3T/8 and T/2, corresponding to a partial closure of the upper discharge valve. The aspirating valve (blue line in the third subplot) exhibits instability during fluid suction, resulting in a less distinct closure that does not significantly impact the incoming flow rate evolution.

Conversely, the 3D results (right subplots) demonstrate more coherent flow dynamics. The discharge valve flow rates are slightly below theoretical expectations (indicated by the comparison between solid and dashed lines in the central subplot). Additionally, the non-return valves exhibit a more dynamic response characterized by an initial rapid closure followed by two swift rebounds (or valve tap effects). A similar dynamic pattern is observed in the aspirating valve during the second half of the cycle, spanning from the top to bottom dead center of the diaphragm stroke

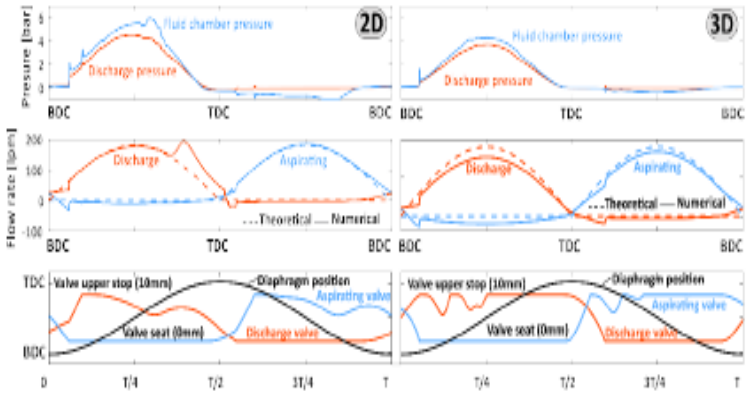

Figure 9. Comparison of temporal evolutions of the pressure, flow rate and check valves response during the diaphragm cycle between 2D (left) and 3D (right) results, in the case of high air-supplied pressure.

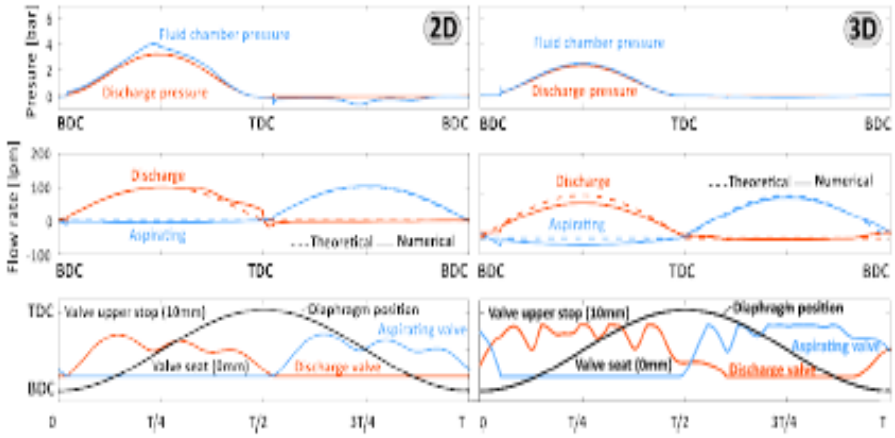

Figure 10. Comparison of temporal evolutions of the pressure, flow rate and check valves response during the diaphragm cycle between 2D (left) and 3D (right) results, in the case of low air-supplied pressure.

4.3.2. Evolution of the Opening in the Non-Return Valves: Comparison of 2D and 3D Simulations

A detailed examination of the oscillatory behavior of the check valves under high driving frequency conditions during standard operation is presented in Figures 11 (discharge valve) and 12 (aspirating valve). These figures illustrate the partial closures of the valves through instantaneous flow field contours depicting velocity magnitude around the valve balls, providing enhanced physical insight. Additionally, the temporal evolution of the instantaneous forces acting on the balls is included to elucidate the observed fluctuations.

For the discharge valve (Figure 11), the 2D simulations predict a single oscillation near the end of the discharge hemicycle, correlated with an abrupt increase in the force exerted on the ball. Initially, the membrane stroke induces complete displacement of the ball (depicted in the first snapshot), after which the ball begins to move downward. At this stage, two high-velocity jets form around the ball (second snapshot), causing a local pressure drop and generating significant suction that tends to re-open the valve gap (third snapshot). Finally, as the forward stroke concludes, the ball returns to its seat (fourth snapshot). It is important to note that the formation of these high-velocity jets around the 2D circular representation of the ball is unrealistic and is primarily a consequence of geometric constraints imposed by the two-dimensional domain.

In contrast, the 3D simulation results (visualized through a transverse section in Figure 11) show a nearly instantaneous valve opening (first snapshot), followed by a rapid partial closure (second

snapshot). This closure is quickly mitigated by the development of a high-velocity region near the ball (third snapshot) as the forward stroke approaches its maximum acceleration at T/4T/4T/4. Subsequently, a second rebound is stabilized due to reinforcement from the incoming fluid propelled by the membrane motion, as evidenced by the prominent high-velocity region adjacent to the ball. This jet-induced suction sustains the valve in an open state and maintains a high force on the ball (fourth snapshot) during the latter half of the hemicycle

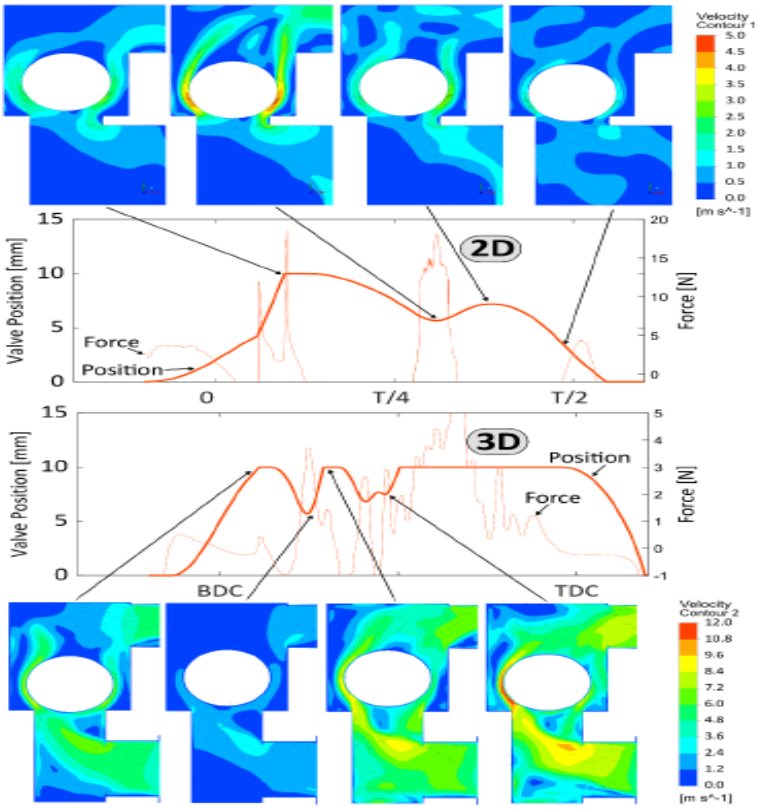

Figure 11. Response of the discharging non-return valve over the operative cycle for high air-supplied pressure. Comparison of 2D (top) and 3D (bottom) computations.

Figure 12 provides similar conclusions with respect the aspirating valve. In this case, the ball dynamics and the surrounding flow patterns are induced by the under pressure associated to the backward stroke. Consequently, the flow patterns are more uniform and high velocity jets are less pronounced with more evenly distributions around the check valve.

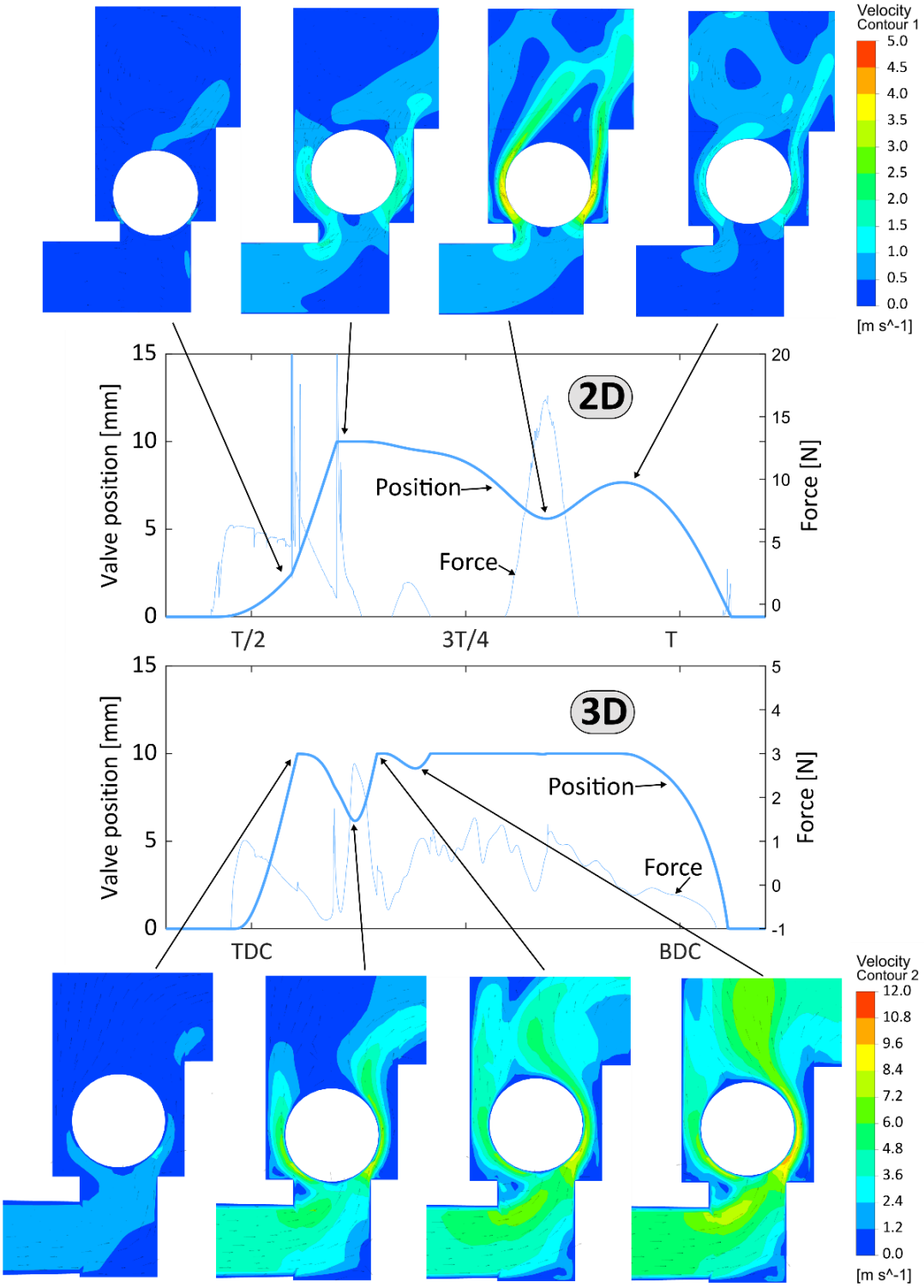

Figure 12. Response of the aspirating non-return valve over the operative cycle for low air-supplied pressure. Comparison of 2D (top) and 3D (bottom) computations.

4.3.3. Evolution of the flow patterns within the pump internal cavities: comparison of 2D and 3D maps

The comparison of 2D and 3D models is finished addressing the differences in the internal flow patterns within the pump in the case of a high air-supplied pressure (@6 bar) for standard operation (figures 13 and 14 respectively).

Firstly, figure 13 shows the description of the 2D flow patterns (contours of velocity magnitude) at four intermediate positions of the operating cycle. Only at t=T/4 the exhausting valve is partially opened; in the rest of the snapshots, it is practically closed. It is quite significant the

appearance of several recirculating cells of fluid in the internal passages; especially in the final contour at the BDC of the diaphragm (t=T), with up to 5 recirculating cells. Note also the flow separation in the outlet manifold at t=T/4 and the accurate guidance of the suctioning flow when it is introduced in the working chamber of the membrane (t=3T/4).

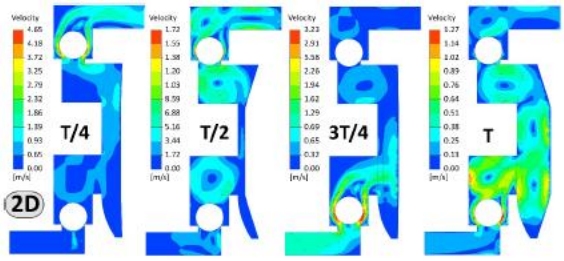

Figure 13. 2D description of flow patterns for high air-supplied pressure.

On the contrary, results in figure 14 does not present any significant flow recirculation in the domain during the whole cycle for 3D computations. Rotational components of the flow velocity at the outlet seem to have been also mitigated. In addition, the highvelocity jets developed around the balls in the check valves are clearly displaced towards the left in the case of the discharging valve and the right in the aspirating valve. This is clearly an effect induced by the piston-like diaphragm when suctioning or driving the flow. Note also that 3D results exhibit lower stagnation conditions than 2D maps.

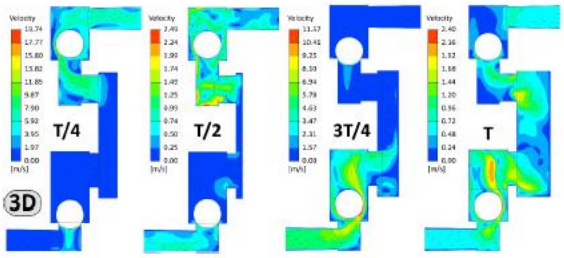

Figure 14. 3D description of flow patterns for high air-supplied pressure.

4.4. Free-Delivery Conditions

When maximum output flow rates are required, diaphragm pumps are typically operated under free-delivery conditions, a scenario commonly encountered during tank draining. Under these conditions, the pump becomes more susceptible to internal instabilities and oscillations, which lead to ball valve tapping and increased vibration due to the higher frequencies involved (up to 2.8 Hz). The numerical results presented in this section are exclusively from the 3D model simulations.

4.4.1. Evolution of Discharged Flow Rate and Pressure as a Function of the Non-Return Valves' Response

Figure 15 illustrates the temporal evolution of the pressure within the working chamber and the corresponding delivered flow rate under high air-supplied pressure (left plots). The pressure within the diaphragm cavity reflects the pressure losses in the internal pump circuit, as the discharge pressure is atmospheric. Notably, pressure peaks under free-delivery conditions are more pronounced compared to standard operation. Furthermore, during the aspiration phase of the working chamber (indicated by the blue line in the top left plot), significant under-pressures are observed, approaching -1 bar, which increases the susceptibility of the pump to cavitation inception. Additionally, volumetric losses are elevated relative to those under standard operating conditions.

The right plots in Figure 15 depict the dynamic response of the valve balls, showing their positions (solid, thick lines), velocities (solid, thin lines), and the corresponding hydrodynamic forces exerted by the fluid (dashed lines). The oscillations of the balls correspond to maximum

velocities on the order of 1 m/s, with peak forces reaching approximately 100 N, predominantly occurring during the closure of the aspirating valve. The data further reveal a delay of approximately one-eighth of the cycle period for the balls to achieve complete closure, indicating that valve closure is not instantaneous

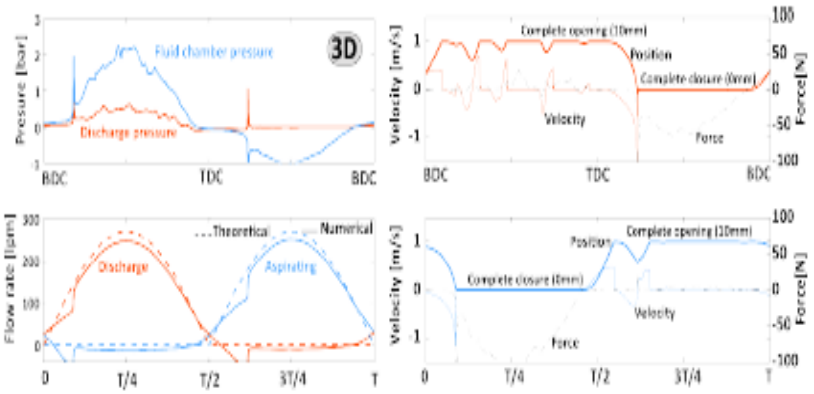

Figure 15. Temporal evolution of pressure and flow rate (left) and response of the no return valves (right) in the case of free delivery for high air-supplied pressure.

Additionally, figure 16 presents similar results but now in the case of a low air-supplied pressure. The pressure in the working chambers is significantly lower, so the volumetric efficiency is clearly improved. The under pressure during the aspiration stroke is also relaxed. Concerning the instabilities in the balls, the evolution in the exhausting and aspirating values differ notably. The exerted forces are also reduced (below 50 N) due to the less demanding conditions.

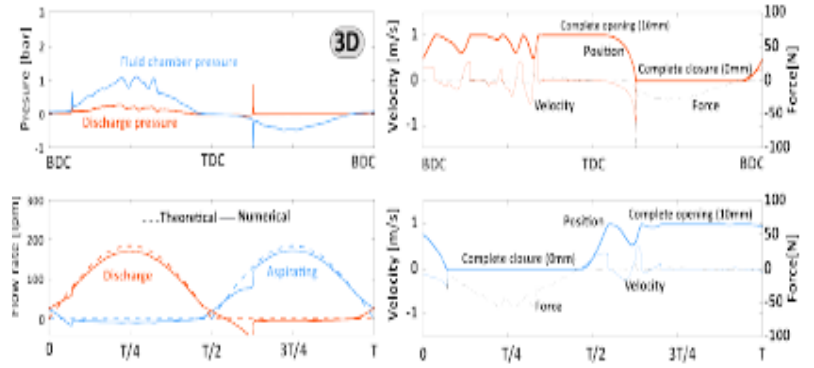

Figure 16. Temporal evolution of pressure and flow rate (left) and response of the nonreturn valves (right) in the case of free delivery for low air-supplied pressure.

4.4.2. Evolution of flow contours in the cavities under free-delivery conditions.

Figure 17 illustrates the evolution of the velocity maps in the working chamber (3D results only), which can be compared to previous results shown in Figure 14 in the case of standard operation. Overall patterns are similar, but higher gradients are identified in the case of freedelivery condition. In particular, the velocity gradients nearby to the discharge valve at t=T/4 are significantly higher. Also, at t=3T/4, the valve side close to the diaphragm exhibits higher velocities as a consequence of the higher driving frequency of the piston.

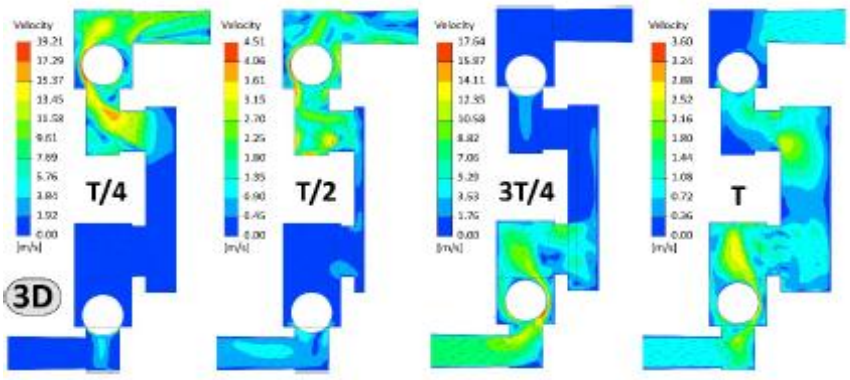

Figure 17. 3D description of flow patterns under free-delivery conditions.

To conclude, Figure 18 presents an additional visualization depicting the principal streamlines emanating from the reciprocating diaphragm within the pump cavities during both the forward and backward strokes. This figure offers a comprehensive three-dimensional perspective on the complex flow patterns occurring around the non-return valves. The left panel clearly identifies a recirculation zone upstream of the discharge valve, accompanied by a region of high rotational flow within the discharge manifold. Conversely, the right panel illustrates a lower vorticity downstream of the aspirating valve, attributable to the increased available space which facilitates a more uniform suction flow induced by the piston. Moreover, minimal recirculation is observed upstream of the aspirating valve. Both images also highlight internal flow leakages occurring at the ball seats, resulting from the partial re-opening of the valves

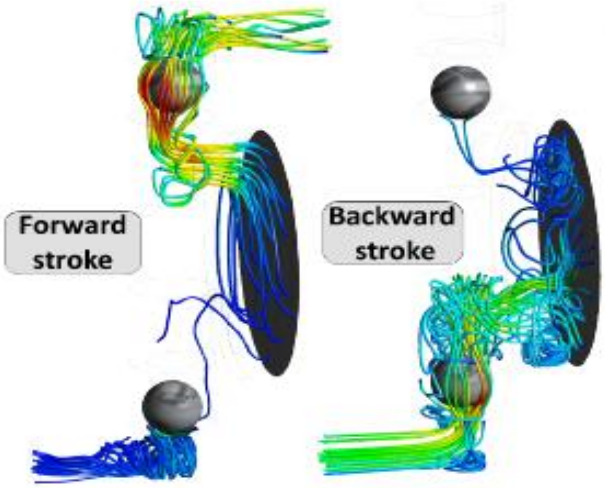

Figure 18. Streamlines in the internal cavities of the pump. Comparison of forward (left) and backward (right) strokes at free-delivery conditions.

4.5. Deformable (Real) Diaphragm vs. Piston-like (Approach) Diaphragm

The study concludes by comparing the overall results obtained from the 3D numerical model incorporating the deformable diaphragm with those previously derived using the piston-like diaphragm approach. The primary aim is to assess whether the additional computational expense associated with the remeshing technique is justified, or if the simplified 3D cylindrical model provides sufficiently accurate predictions.

Figure 19 (right column) demonstrates that the overall behavior of the principal fluid-dynamic variables is quite similar between the two models. Nevertheless, the pressure within the diaphragm cavity exhibits a less sinusoidal pattern in the deformable diaphragm model, attributable to the early deceleration of the internal rigid circular plate. Consequently, a plateau appears in the pressure distribution, reflecting the reduced displacement during the final stages of the diaphragm stroke. This phenomenon affects the dynamics of the discharge non-return valves,

resulting in only two valve re-openings. Conversely, the response of the aspirating valve remains nearly identical across both models. Notably, the volumetric efficiency is significantly enhanced when employing the deformable diaphragm

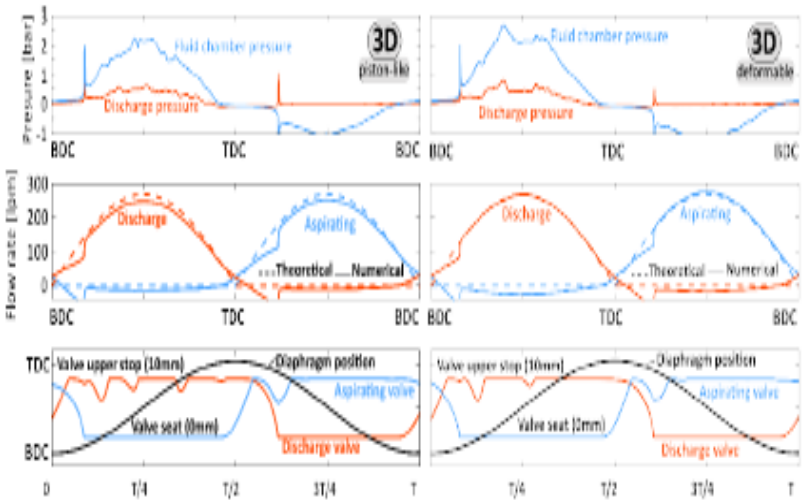

Figure 19. Comparison of temporal evolutions of the pressure, flow rate and check valves response during the diaphragm cycle between 3D, piston-like model (left) and 3D deformable diaphragm (right) results.

Finally, Figure 20 illustrates the differences in flow patterns, depicted through velocity fields, between the deformable and piston-like diaphragm models. The left panel presents velocity contours at T/4, corresponding to the peak forward stroke impulse, highlighting how the diaphragm-driven flow traverses the discharge valve. In the deformable diaphragm model, the flow is more effectively directed into the outlet port, forming a well-defined and gradually expanding high-velocity jet around the valve ball. Conversely, the piston-like model exhibits a notable region of recirculation within the rectangular cavity connecting the working chamber to the outlet manifold, thereby accounting for the higher volumetric losses observed in Figure 19. On the right panel, velocity maps at 3T/4 during the backward stroke reveal only minor differences between the two models. A key distinction is that the deformable diaphragm provides increased space in the lower chamber region, allowing a more gradual distribution of the suction-induced pressure gradient. This facilitates improved aspirating conditions, reflected in reduced flow leakage through the inlet check valve

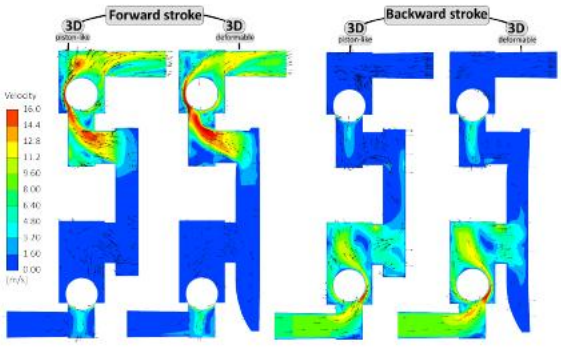

Figure 20. Comparison of flow patterns in the cavities between 3D piston-like model and 3D deformable diaphragm model.

5. Conclusions

A comprehensive three-dimensional, unsteady CFD model employing dynamic meshes has been developed and validated for the simulation of Air-Operated Double Diaphragm (AODD) pumps

under various operating conditions. This advanced 3D model builds upon a previously established two-dimensional numerical methodology recently presented by the authors. The new three-dimensional results were systematically compared against prior 2D data with respect to overall pump performance, volumetric efficiency, and the dynamic response of the non-return valves, thereby confirming the advantages of fully 3D modeling for accurately capturing the complex fluid-structure interactions inherent in these positive displacement pumps.

To optimize computational efficiency, an initial piston-like diaphragm approximation was utilized, replicating the volumetric displacement of the real deformable diaphragm and enabling the use of more computationally economical layering remeshing algorithms. Subsequently, a flexible, deformable diaphragm model was developed for completeness, revealing that the piston-like approach reliably reproduces the overall behavior and fundamental performance metrics of the system's components.

Experimental validation demonstrated satisfactory agreement between the 3D numerical predictions and measured performance curves, substantiating the appropriateness of the chosen mesh resolution, mesh quality, and time step size. Although local pressure measurements within the diaphragm cavity showed temporal discrepancies during the operating cycle, the time-averaged pressure trends were accurately captured. Under standard operating conditions, low air-supplied pressures (approximately 2 bar) led to increased instabilities and frequent ball valve tapping—particularly in the discharge valve—with up to four partial re-openings observed. Increasing the supplied pressure to 6 bar mitigated these oscillations, reducing re-openings to two during the initial forward stroke and improving volumetric efficiency.

Significantly, the 2D model exhibited excessive damping, underestimating the dynamic fluid-structure interactions between the balls and fluid flow. In contrast, the 3D model provided a more faithful and detailed representation of rapid inertial effects and valve dynamics. Under free-delivery conditions, the 3D model predicted behavior consistent with standard operation but highlighted pronounced pressure drops within the diaphragm cavity during the suction stroke, with near-vacuum pressures that raise concerns for cavitation inception. Volumetric losses were also elevated relative to standard conditions, consistent with the pump's efficiency map.

Finally, it was consistently observed that valve instabilities were more pronounced in the discharge valve than in the inlet valve. The inlet valve exhibited superior sealing performance, with only minor partial re-openings occurring near the onset of the backward stroke. This finding provides valuable insights for guiding the design, material selection, and maintenance strategies of critical pump components

References

1. Aldi, N., Buratto, C., Pinelli, M., Spina, P.R., Suman, A., Casari, N., 2016. CFD analysis of a non-Newtonian fluids processing pump. Energy Procedia 101, 742–749.
2. Altare, G., Rundo, M., CFD analysis of gerotor lubricating pumps at high speed: Geometric features influencing the filling capability. In: Proceedings of the ASME/BATH 2015 Symposium on Fluid Power and Motion Control, Chicago, IL (USA), October 12–14, 2015.
3. ANSI/HI. 10.1-10.5, 2010. Air Operated Pumps for Nomenclature, Definitions, Application and Operation. Hydraulic Institute. ANSI/HI. 10.6, 2004. Air Operated Pump Tests. Hydraulic Institute. ANSYS-FLUENT Meshing User's Guide. Release 16.2.
4. ANSYS, Inc. 2015. ANSYS-FLUENT User's Guide. Release 16.2. ANSYS, Inc. 2015. Bahrton, S., 2002. Reversing Valve for a Diaphragm Pump. US Patent 6419463 B1.
5. Beune, A., Kuerten, J.G.M., van Heumen, M.P.C., 2012. CFD analysis with fluid-structure interaction of opening high-pressure safety valves. Comput. & Fluids 64, 108–116.

6. Farrell, R., Ezekoye, L.I., Rain, M., Check valve flow and disk lift simulation using CFD. In: Proceedings of ASME Pressure Vessels and Piping Conference, Hawaii (USA), July 16–20, 2017.

7. Frosina, E., Senatore, A., Buono, D., Stelson, K.A., Wang, F., Mohanty, B., Gust, M.J., Vane pump power split transmission: Three dimensional computational fluid dynamic modeling. In: Proceedings of the ASME/BATH 2015 Symposium on Fluid Power and Motion Control, Chicago, IL (USA), October 12–14, 2015. González-Moratiel, A., 2013. Double-Membrane Central-Flow Pump. EP Patent 2573397 A1.

8. Hwang, I.S., Park, S.J., Oh, W., Lee, Y.L., 2017. Linear compressor discharge valve behavior using a rigid body valve model and a FSI valve model. Int. J. Refrig. 82, 509–519.

9. Iannetti, A., Stickland, M.T., Dempster, W.M., 2014. A computational fluid dynamics model to evaluate the inlet stroke performance of a positive displacement reciprocating plunger pump. Proc. IMechE A 228 (5), 574–584.

10. Iannetti, A., Stickland, M.T., Dempster, W.M., 2015. A CFD study on the mechanisms which cause cavitation in positive displacement reciprocating pumps. J. Hydraul. Eng. 1 (1), 47–59.

11. Iannetti, A., Stickland, M.T., Dempster, W.M., 2016. A CFD and experimental study on cavitation in positive displacement pumps: Benefits and drawbacks of the 'full' cavitation model. Eng. Appl. Comput. Fluid Mech. 10 (1), 57–71.

12. Kumar, S., Bergada, J.M., Watton, J., 2009. Axial piston pump grooved slipper analysis by CFD simulation of three-dimensional NVS equation in cylindrical coordinates. Comput. & Fluids 38, 648–663.

13. Ma, Y., Ni, Y., Zhang, H., Zhou, S., Deng, H., 2018. Influence of valve's lag characteristic on pressure pulsation and performance of reciprocating multiphase pump. J. Petrol. Sci. Eng. 164, 584–594. Menéndez Blanco, A., 2017.

14. Numerical Modelling of Volumetric Diaphragm Pumps (Ph.D. thesis). University of Oviedo, Spain (in Spanish). Menéndez-Blanco, A., Fernández Oro, J.M., 2012. Unsteady numerical simulation of an air-operated piston pump for lubricating greases using dynamic meshes. Comput. & Fluids 57, 138–150.

15. Menéndez-Blanco, A., Fernández Oro, J.M., Meana-Fernández, A., 2019. A numerical methodology for the CFD simulation of diaphragm volumetric pumps. Int. J. Mech. Sci. 150, 322–336.

16. Pan, X., Yang, S., Shi, Y., Liu, Y., 2019. Investigation on the dynamic characteristics of port valves in a diaphragm pump for exhaust gas treatment system by FSI modeling. IEEE Access http://dx.doi.org/10.1109/ACCESS.2019.2914282. Ragoth, R.S., Nataraj, M., 2012. Study on performance of plunger pump at various crank angle using CFD. Eng. Sci. Technol. Int. J. 2 (4), 549–553.

17. van Rijswick, R., Talmon, A., van Rhee, C., 2016. Fluid structure interaction (FSI) in piston diaphragm pumps. Can. J. Chem. Eng. 94 (6), 1116–1126. SAMOA Flow, Online catalogue for Diaphragm Pumps. http://www.samoaindustrial.com/flow/catalogo_directflo_en.html. (Accessed 21 November 2019).

18. Srikanth, C., Bhasker, C., 2009. Flow analysis in valve with moving grids through CFD techniques. Adv. Eng. Softw. 40 (3), 193–201. Tan, Q., Pan, S., Feng, Q., Yu, X., Wang, Z., 2014.

19. Fluid–structure interaction model of dynamic behavior of the discharge valve in a rotary compressor. Proc. IMechE E 229 (4), 280–289.

20. Tao, W., Guo, Y., He, Z., Peng, X., 2018. Investigation on the delayed closure of the suction valve in the refrigerator compressor by FSI modeling. Int. J. Refrig. 91, 111–121.

21. Wang, G., Zhang, L., He, X., Lei, Z., Hu, G., Li, R., Wang, Y., 2015. Dynamic behavior of reciprocating plunger pump discharge valve based on fluid structure interaction and experimental analysis. PLoS One 10 (10), 1–20.

22. Wei, G., 2006. An Implicit Method to Solve Problems of Rigid Body Motion Coupled with Fluid Flow. Technical note, FSI-05-TN76. Flow Science Inc.. Zhang, S.C., Zhang, Y.L., Fang, Z.M., 2012. Numerical simulation and analysis of ball valve three-dimensional flow based on CFD. In: IOP Conference Series: Earth and Environmental Science, vol. 15, 052024